scientific reports

Check for updates

OPEN

Anisotropic piezoresistive response of 3D-printed pressure sensor based on ABS/MWCNT nanocomposite

Luciano J. B. Quaresma[1,2]✉, Dhonata S. C. Oliveira[1,2], Rosielem S. Dias[1,2], Kelly C. Alves[1], Luiz G. D. de Barros[4,7], Gustavo Pessin[5,6,7], Amilton Sinatora[7], Waldeci Paraguassu[1] & Marcos A. L. dos Reis[1,2,3]

Nanocomposites based on carbon nanotubes (CNTs) are suitable for sensors, due to matrix ability to incorporate nanotube properties. Thus, we developed a low-cost, nanostructured poly(acrylonitrile-butadiene-styrene) (ABS) polymer piezoresistive sensor produced by additive manufacturing. For this, solution layers of acetone, dimethylformamide and CNTs functionalized with carboxylic acid were pulverized on an ABS substrate using an aerograph. Electrical characterization revealed an anisotropic piezoresistive response of the material, induced by the printing lines direction. Field Emission Gun-Scanning Electron Microscopy showed the nanostructured film spreading after five layers of CNTs as well as the random entanglement of nanotubes on parallel and perpendicular 3D-printed ABS substrates. Raman spectroscopy indicated compression and p-type doping of CNTs in interaction with the polymer, as seen mainly by the blueshift of the G and 2D subbands. The results show that the material is promising for pressure sensors, with potential applications in robotic haptic feedback systems.

Nanomaterials have at least one dimension smaller than 100 nm, which implies on a greater surface-to-volume ratio and usually in the prevalence of quantum effects, leading to superior and/or unusual properties compared to their bulk counterparts[1,2]. Carbon-based nanomaterials, e.g. fullerenes, nanodiamonds, graphene and carbon nanotubes (CNTs), have attracted great academic attention due to their versatility originated by the different carbon atom hybridizations and capacity to bond to nearly all other elements[3]. This leads to nanomaterials with mechanic, electric, chemical, etc. properties that are very interesting to sensing applications, such as pressure[4,5], deformation[6,7] and vibration[8,9], even more so considering the enhanced response and recovery times and sensitivity of these materials[3]. However, for practical and scalable applications it is convenient to use nanomaterials in nanocomposites, due to the easier processability of usual materials as matrixes, e.g. metals, ceramics and polymers, at the cost of some reduction of the nanomaterial properties[1–3].

In this context, carbon nanotubes polymeric nanocomposites are suitable for piezoresistive sensors, due to the elasticity of the polymers and the CNTs electrical properties[10–13]. For instance, multi-walled carbon nanotubes (MWCNTs) with many walls reach electrical conductivities between 10^3 and 10^5 S/m[12,13]. This allows the formation of nanotube conduction channels in nanocomposites, leading to piezoresistivity influenced by several factors, with emphasis on CNTs dispersion. Nanotubes tend to agglomerate due to van der Waals interactions, which can degrade their electrical properties[10–13]. Better dispersing the CNTs in suitable solutions during the nanocomposite production process could avoid this, which is facilitated by the functionalization of the nanotubes[14,15]. For example, carboxylic acid functionalization introduces COOH radicals on CNTs tips and outer walls forming MWCNTs-COOH, which enhances their solubility and dispersion in polar solvents, such as water, acetone and dimethylformamide (DMF)[15,16]. Polymers such poli(acrylonitrile-butadiene-styrene) (ABS) are also soluble in such solvents, making this a route of piezoresistive nanocomposites production[17,18].

[1]Graduate Program in Materials Science and Engineering, Federal University of Pará, Ananindeua, PA, Brazil. [2]3D Nanostructuring Laboratory, Federal University of Pará, Belém, PA, Brazil. [3]Graduate Program in Amazon's Natural Resources Engineering, Federal University of Pará, Belém, PA, Brazil. [4]Mechanical Engineering Department, São Carlos School of Engineering, University of São Paulo, São Carlos, SP, Brazil. [5]Institute of Exact and Natural Sciences, Federal University of Pará, Belém, PA, Brazil. [6]Federal University of Ouro Preto, Ouro Preto, MG, Brazil. [7]Instituto Tecnológico Vale, Ouro Preto, MG, Brazil. ✉email: luciano.quaresm@gmail.com

To illustrate, CNT-based piezoresistive nanocomposites were produced with several polymeric matrixes, such as thermoplastic polyurethane (TPU)[19]; waterborne polyurethane (WPU)[20]; polyimide[21]; polydimethylsiloxane (PDMS)[22]; polyvinylidene fluoride (PVDF)[23]; epoxy resin[24]; and silicon[25]. These materials were produced mainly by the solvent route, however fused deposition modeling (FDM) additive manufacturing is a promising alternative method for piezoresistive polymeric nanocomposites preparation. The production of filaments of CNT-based nanocomposites with thermoplastic polymers, e.g. styrene-ethylene-butylene-styrene (SEBS)[26], polypropylene[27], TPU[28] and ABS[29], enables the practical use of 3D printing for designing functional nanostructured devices.

Results

Sensing elements production

In this work, we developed a 3D-printed load cell using commercial ABS polymer filament and MWCNTs-COOH, as shown by the 3D model in Fig. 1a. The sensing element consists of a 3D-printed ABS substrate, a layer of CNTs and an encapsulation layer of ABS with conductive silver ink coating as electrodes, as schematized in Fig. 1b. Two groups of three samples were produced: one with printing lines parallel to the direction connecting the electrodes, and the other with printing lines perpendicular to this direction. Depending on the orientation, the printing lines either form direct paths or act as obstacles between the electrodes on the sample's surface, influencing the electrical behavior. Additionally, three more samples per group were produced with applied electric field to align the CNTs, which could enhance electrical conductivity[30,31]. Moreover, the electric field generates heat via the Joule effect[32,33], potentially improving adhesion between the ABS substrate and the CNTs. Figure 1c shows a photograph of the resulting 12 sensing element samples used for electrical characterization.

For the deposition of the CNTs layer, a solution of Acetone-DMF/MWCNTs-COOH was applied using an aerograph. The process was made in cycles, each comprising the solution spraying, the application of a direct current electric field of approximately 38.5 kV/m and a 10-minute drying under ambient conditions. The electrical resistance was measured after each cycle, as illustrated in Fig. 1d, for A and B parallel printed samples and for C and D perpendicular printed samples (B and D samples were prepared with applied electrical field). This analysis showed the electrical percolation of the material after the third layer of solution, as the resistance drops from 10^{12} to about 10^{6} W. This process occurs due to the formation of conduction channels on the ABS surface, as described by statistical models for a growing number of sites occupied by conductive nanoparticles[10,11]. Upon reaching a critical volume fraction of nanoparticles, the material surpasses its percolation threshold and become conductive. Generally, polymeric CNTs nanocomposites have this threshold at 1 ~ 4% of nanotubes

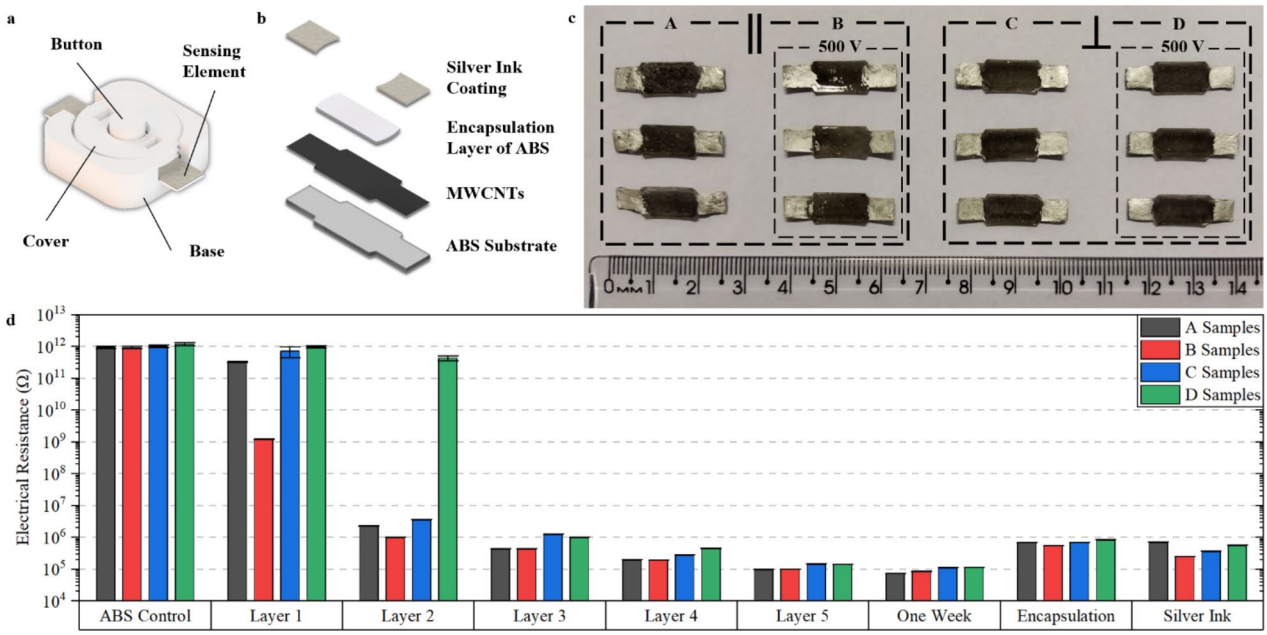

Fig. 1. Sample's preparation. (**a**) 3D model of the load cell with a cover, a button to transfer load to the sensing element and a base to control its deformation. (**b**) schematic representation of the sensing element highlighting the ABS substrate, the CNTs layer, the ABS encapsulation layer and the conductive silver ink coating for the terminals. (**c**) photograph of the 12 samples for electrical characterization. Samples from groups A and B feature parallel printing lines relative to the longest dimension, while samples from groups C and D feature perpendicular printing lines. Samples in groups B and D were produced with applied electrical field. (**d**) mean electrical resistance of each sample group, along with pure ABS control samples, for 1–5 layers of CNTs and subsequent measurements after one week of drying in ambient conditions, an encapsulation layer of ABS and application of a conductive silver ink coating. Each column represents the mean electrical resistance of three different samples from each group and the error bars represent the respective mean standard deviations. The values for each individual sample were obtained from the mean of 10 measurements.

mass percentage[19–29]. However, with our method, the final mass percentage of CNTs was 0.22 ± 0.30%, as only the sensing element surface was nanostructured. This resulted in an average usage of 0.17 ± 0.19 mg of nanotubes on a 3D-printed ABS substrate with 62.24 ± 0.15 mg.

After five layers, groups A and B exhibited lower mean electrical resistances (97.75 ± 0.11 kW and 100.01 ± 0.03 kW, respectively) than groups C and D (146.73 ± 0.035 kW and 141.06 ± 0.012 kW). This discrepancy is attributed to the sensing elements geometry, as the direct paths between terminals formed by the parallel printing lines facilitate the formation of CNTs conduction channels on the polymer surface. Conversely, the perpendicular printing lines of the other group acted as barriers to formation of the conduction channels, resulting in higher electrical resistance. Furthermore, when subjected to electrical field, the resistance of parallel printed samples decreased more rapidly while the opposite happened for perpendicular printed samples, particularly in the first layers. This suggests 3D printing induces anisotropy in the samples' electrical resistance.

Additional measurements were made after one week of drying in ambient conditions, an encapsulation a layer of ABS and a conductive silver ink coating on the terminals. For all groups, the electrical resistance decreased after one week, possibly from the evaporation of solvent residues. After encapsulation, the electrical resistance increased, likely due to the elimination of some conduction channels and the reduction of doping, as CNTs are sensitive to air oxygen, especially when functionalized[34,35]. Notably, the group A samples exhibited lower electrical resistance than group B after one week of drying, but higher resistance following encapsulation. This suggests that group A may have initially formed more conductive channels, but these channels were likely less stable, leading to a greater increase in resistance after encapsulation. Subsequently, the conductive silver ink reduced electrical resistance by improving contact with the measuring equipment. Groups B and C showed lower mean electrical resistances for each orientation, respectively 251.58 ± 0.034 kW and 366.51 ± 0.13 kW.

To assess the stability of the signal acquired from the samples, the Fig. 2 illustrates the mean relative standard deviations (RSD) of measurements for the fifth layer of CNTs and under these three last conditions. While the electrical resistance decreases after one week, there is an increase on the RSD for groups B, C and D, implying in a decrease of their stability. Conversely, the error is reduced after the encapsulation, despite the higher electrical resistance observed. This suggests that, in addition to the CNTs doping reduction, this ABS layer also enhances the stability of the sample's response. Finally, after the conductive silver ink, groups B and C exhibited lower RSD, indicating improved stability and likely a better piezoresistive response. This indicates that the electrical field improved the stability for samples with parallel printing lines. Due to the direct paths on which the conduction channels are formed, the electric field possibly further organized the nanotubes. Conversely, the opposite effect happened on the other group, on which the perpendicular printing lines act as barriers to the formation of conduction channels between the terminals. In this case, the electric field possibly disorganized the conduction channels due to the barriers. These results indicate that the group A conduction channels were indeed less stable, as this group displayed the highest final mean RSD. The results also suggest further control over the electrical resistance anisotropy in function of the printing lines orientation.

FEG-SEM microscopy

The morphological characterization of the material corroborates the electrical results. With each layer of solution applied, the surface area coated by the CNTs increases, leading to the percolation of the material. As a result, a nanostructured film formed, as depicted in Fig. 3a and b for a parallel and a perpendicular 3D-printed sample, respectively. Micrographs indicate that the films were not homogeneous, with regions showing lower concentrations of CNTs appearing as darker areas, particularly noticeable on the perpendicular printed sample, which also exhibited more 3D printing defects.

Notably, globular structures were visible even at low magnification, serving as indicators of film spreading, as they are formed by CNT agglomerates. This is illustrated in Fig. 3c, where these structures are mainly observed on the brighter regions of the surface with higher CNT concentrations. In Fig. 3c inset, the entanglement of

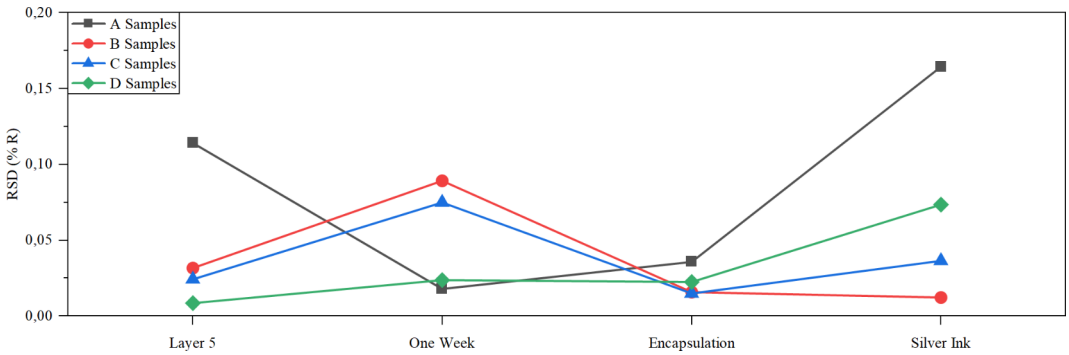

Fig. 2. Sample's electrical signal stability. Mean relative standard deviations (RSD) for electrical resistance measurements of groups A, B, C and D after the fifth layer of CNTs, following one week of drying, the encapsulation layer of ABS and the application of a conductive silver ink coating. B and C samples displayed higher final stability for each printing lines orientation. All RSDs were calculated from 10 electrical resistance measurements of individual samples and the mean values were obtained from the three different samples of each group.

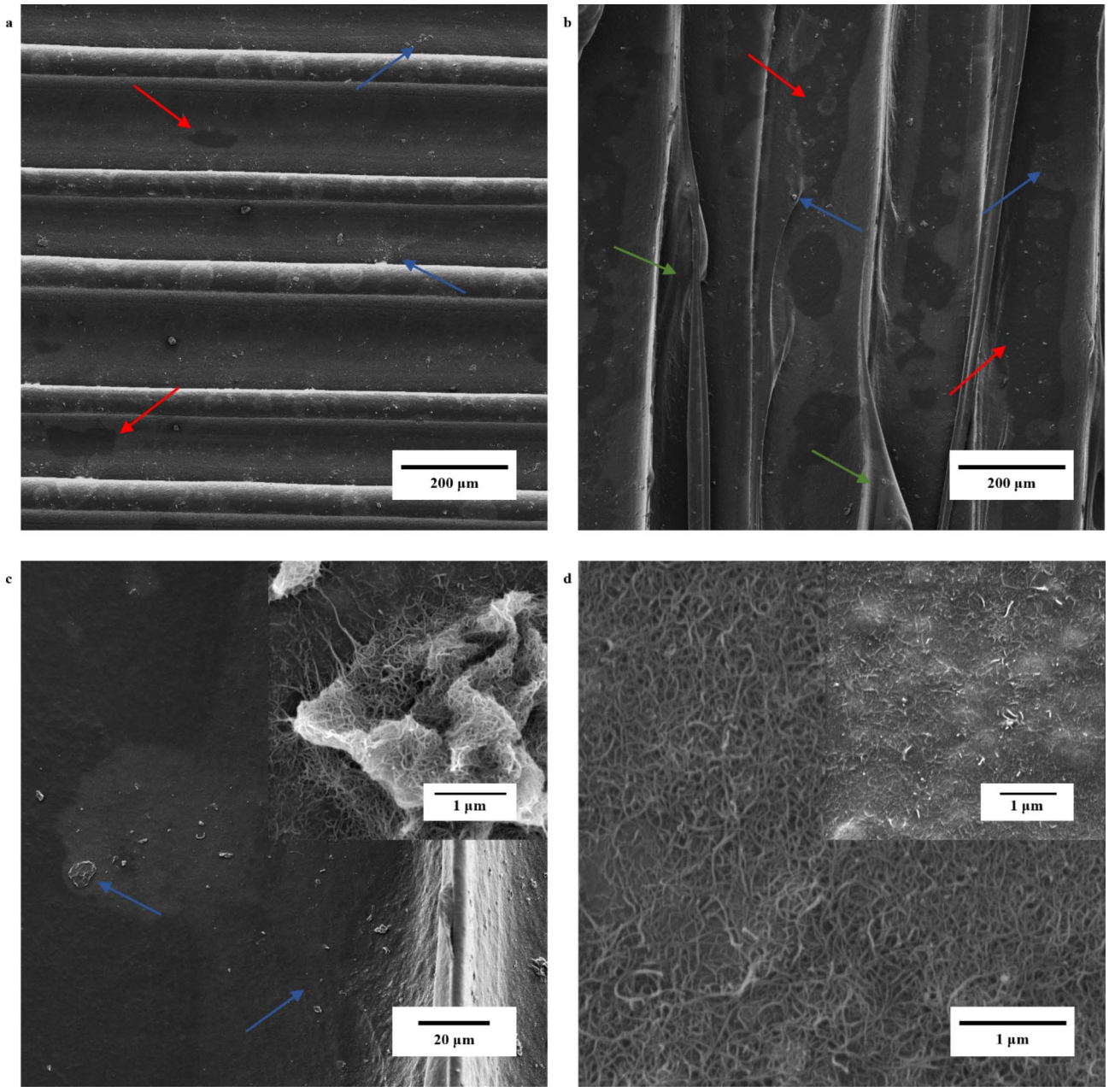

Fig. 3. ABS/COOH-MWCNTs FEG-SEM micrographs. (**a**) low magnification 227x image of a group B sample, highlighting regions with lower concentrations of CNTs (red arrows) and globular structures formed by nanotube agglomeration (blue arrows). (**b**) low magnification 277x image of a group D sample, displaying similar features to the group B sample, with larger regions of lower CNT concentration (red arrows), globular structures (blue arrows), and 3D printing defects (green arrows). (**c**) interface between regions with different CNTs concentrations in 1.85 kx magnification image, exhibiting globular structures predominantly in the regions with higher CNTs concentration (blue arrows). High magnification 70.6 kx inset shows a detailed view of one such structure, displaying the agglomeration of CNTs. (**d**) surface morphology in 55.3 kx magnification image displaying the random distribution of nanotubes in the conduction channels. The inset at 55.4 kx magnification reveals the surface morphology of a sample with a single layer of CNTs, with some nanotubes appearing fused to the ABS polymer substrate, suggesting the formation of a nanocomposite.

nanotubes forming these structures becomes apparent. Apart from these agglomerates, the film exhibited the morphology shown in Fig. 3d, with a random arrangement of carbon nanotubes forming the conduction channels. The Fig. 3d inset highlights the surface morphology of a sample with a single layer of CNTs, indicating the formation of a nanocomposite as the nanotubes appears to be fused to the ABS substrate. This could be result of a superficial solubilization of the polymer, as the acetone in the CNTs solution is also its solvent.

Raman spectroscopy

The Raman spectra were fitted using Lorentzian subbands, as depicted in Fig. 4a, b and c for commercial ABS, as-received MWCNTs-COOH and the ABS/MWCNTs-COOH nanocomposite, respectively. The detailed results for these materials are provided in Tables 1, 2 and 3 of the Supplementary Information. For the ABS spectrum, seven regions with distinct vibrational modes were identified, labelled from R_1 to R_7. In the first region, vibrational modes were assigned to the styrene benzene ring, including a C-C-C out-of-plane stretching at 989 cm^{-1}, a ring breathing at 1001 cm^{-1} and C-H in-plane deformation at 1030 and 1034 cm^{-1}[36–38]. Region R_2 exhibited a benzene ring out-of-plane C-H deformation mode at 1156 cm^{-1} and C-H in-plane deformation at 1182 and 1189 cm^{-1}, along with a C-C symmetric stretching mode at 1199 cm^{-1} from the alkane chains of the polymer backbone[36,37]. Modes in the region R_3, at 1446 and 1455 cm^{-1}, were attributed to C-C asymmetric stretching mode of benzene ring and CH_2 deformation mode, respectively[36–38].

In region R_4, modes are associated with benzene ring C-C antisymmetric stretching at 1583 cm^{-1} and C-C symmetric stretching at 1601 and 1605 cm^{-1}, appearing in same region of the G band of CNTs[36–38]. Region R_5 exhibited vibrational modes at 1650 and 1667 cm^{-1} attributed to C=C stretching modes of polybutadiene cis and trans isomers, respectively[36–38]. The R_6 mode at 1730 cm^{-1}, not commonly identified for ABS, may indicate a peculiarity of the commercial ABS used[36,37]. Similarly, the absence of a vibrational mode around 2239 cm^{-1}, typically present on ABS spectra and assigned to C≡N stretching mode from acrylonitrile, is noteworthy[36–38].

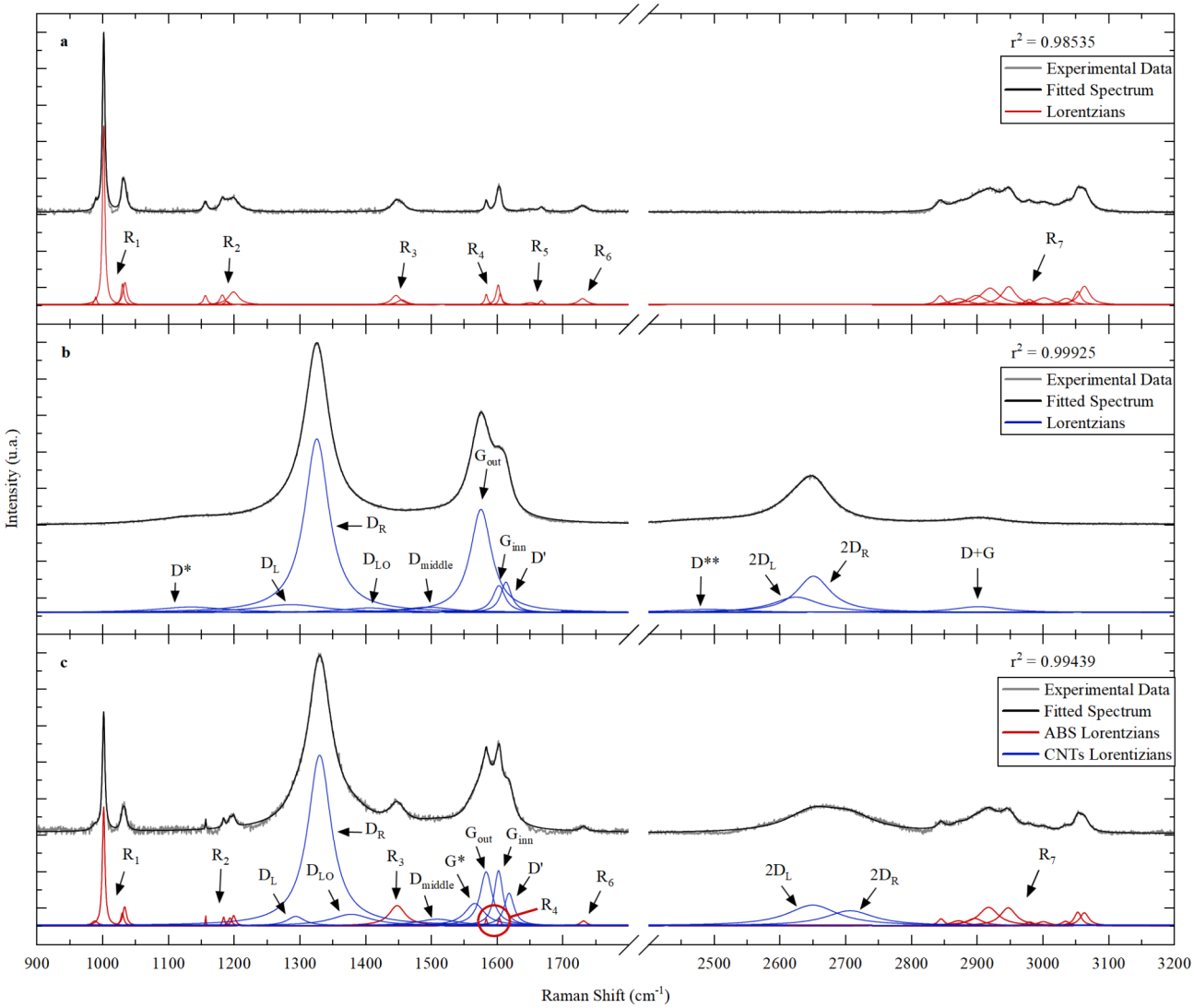

Fig. 4. Deconvoluted Raman spectra. (**a**) Raman spectrum of commercial ABS polymer, fitted with 26 Lorentzian subbands grouped by Raman shift in seven regions. (**b**) Raman spectrum of as-received MWCNTs-COOH, fitted with 14 subbands commonly identified in literature. (**c**) Raman spectrum of ABS/MWCNTs-COOH nanocomposite, demonstrating an overlap of the individual materials' spectra. The data were acquired from 900 to 3200 cm^{-1} and plotted with a break from 1800 to 2400 cm^{-1} due to the absence of vibrational modes. The r^2 values for the fits are shown in their respective figures.

Finally, in region R_7, several modes between 2844 and 3063 cm^{-1} were identified, assigned to various CH and CH_2 vibrations from alkane and alkene chains, as well as from benzene rings[36–38].

In the Raman spectrum of the CNTs, the first-order modes G_{out} and G_{inn}, composing the G band, were identified at 1575 and 1602 cm^{-1}, respectively. These modes are usually distinguishable in MWCNTs and associated with the outermost and the innermost tubes tangential C=C vibrational modes[39–41]. Second-order modes can result from two phonons scatter events or a phonon and an elastic scatter event. In the first case, overtone modes occur with the same phonon scatter modes and combination modes with different ones[39,42]. For the D band, disorder and defects in the CNTs structure induces elastic scatter for second-order Raman modes. These include: D* at 1134 cm^{-1}, potentially associated with longitudinal acoustic (LA) or longitudinal optic (LO) modes, calculated to be around 1200 cm^{-1}[39,43]; D_L and D_R, respectively at 1286 and 1326 cm^{-1}, with high intensities commonly used as indicative of defects, functionalizations and MWCNTs with a large number of walls and diameter[39]; D_{LO} at 1405 cm^{-1}, possibly associated to LO modes; and D' at 1613 cm^{-1}, also associated with defects and functionalizations in CNTs structure[43]. Additionally, the D_{middle} at 1494 cm^{-1} is attributed to the amorphous carbon degree of the sample[40]. At higher frequencies, four second-order two phonon scatter Raman modes are identified: D**, the overtone of D* at 2491 cm^{-1}; $2D_L$ and $2D_R$, the overtones of the D band at 2624 and 2650 cm^{-1}, respectively, associated with the innermost and the outermost tubes; and D+G, the combination mode of D and G bands at 1902 cm^{-1}[39,40,42,43].

The ABS/COOH-MWCNT nanocomposite fingerprint exhibits an overlap of the individual materials' spectra, on which some modes weren't identified, such as C=C stretching modes of polybutadiene from ABS and D*, D** and D+G from the CNTs. This suggests that besides being deposited, the nanotubes also interact with the ABS substrate. This is further supported by the dislocation and overlap of vibrational modes compared to the reference spectra. For instance, D_{LO} and D_{middle} overlapped with the mode from region R_3 of the ABS polymer associated with styrene benzene ring, while the mode attributed to CH_2 deformation was not identified. This behavior may indicate an amorphization induced by the ultrasonication in the solvents. This is further supported by the 5 cm^{-1} blueshift of the disorder-induced D' subband. Additionally, the absence of the CH_2 mode could indicate an interaction with the alkane and alkene chains forming the backbone of the polymer. This is corroborated by the blueshift of two of the modes in R_2 region, also associated to the backbone vibrations, and the negligible dislocation of the CH modes associated with the benzene ring on this region.

In the G band, a change in line shape made it necessary to fit the spectrum with the extra G* subband, which can be attributed to the formation of sp^3 domains of polycyclic aromatic hydrocarbons and covalent functionalizations on the tube's tips[44]. Both processes could be induced by the ultrasonication in acetone and DMF. The G band also presented an overlap of G_{out} with 8 cm^{-1} blueshift at 1583 cm^{-1} and G_{inn} at 1602 cm^{-1} with R_4 modes at 1583 and 1603 cm^{-1}. As the blueshift of the G band typically indicates both compression of the tubes and p-type doping[45–47], these results suggest an interaction between the polymer and the outermost walls of the CNTs, as only G_{out} shifted. This compression may be induced by the entanglement of randomly deposited CNTs on the ABS substrate, while the doping could result from electronic interactions between the functionalized nanotube walls and the polymer chains. Although it is difficult to attribute this blueshift to a specific effect[46,47], a p-type doping is supported by the significant shifts observed in the 2D subbands. Specifically, $2D_L$ was identified at 2650 cm^{-1} and $2D_R$ at 2706 cm^{-1}, with blueshifts of 25 and 56 cm^{-1}, respectively[45–47]. These results corroborate the formation of a nanocomposite as discussed in the FEG-SEM microscopy analysis, due to the electronic interaction between the ABS polymer substrate and the CNTs.

Piezoresistive behavior

The piezoresistive response of the sensors was investigated through cycles of increasing pressure controlled an actuator, ranging from 68.27 ± 0.22 kPa to 363.25 ± 0.39 kPa, with a mean increase of 73.89 ± 1.60 kPa per cycle. Initial tests revealed that samples from the groups B and C exhibited better piezoresistive response for each printing orientation, as displayed in Fig. 5a for two individual samples, one from each group. Across all samples, there was no significant response observed at 68.27 ± 0.22 kPa, indicating an operational range from 139.97 ± 0.46 to 363.25 ± 0.39 kPa. Detailed information regarding mean values per sample group of initial electrical resistance, sensitivity, response time, and recovery time is provided in Table 4 of Supplementary Information.

In the cycles with increasing load, the B group presented higher mean sensitivities in all cycles, reaching 0.75 ± 0.36% at the upper operational range, while C group reached 0.42 ± 0.12%. However, the C group displayed lower mean response times under higher loads in the fourth and fifth cycles, respectively with 1.13 ± 1.09 and 1.02 ± 0.90 s, compared to B group's 6.10 ± 6.35 and 4.52 ± 6.36 s. For recovery times, the B group had lower values, ranging from 2.26 ± 1.87 to 10.84 ± 2.06 s, in contrast to C group's range of 5.76 ± 2.69 to 15.02 ± 1.41 s. These results suggest anisotropy on the piezoresistive behavior of the material, which could be useful for distinguishing mechanical stresses directions. To analyze the piezoresistive response, Fig. 5b displays the quasi-linear increase of sensitivity as the load increases over the cycles for both geometries indicating the distinguishability of loads within the operational range.

To further analyze the stability and repeatability of the piezoresistive response, the same individual groups B and C samples were subject to load cycles with pressure of 363.25 ± 0.39 kPa. The results are illustrated in Fig. 5c and detailed information regarding each group's mean sensitivity and mean response and recovery times is presented in Table 5 of Supplementary Information. The C group presented lower mean sensitivity of 0.38 ± 0.22%, while B group reached 0.50 ± 0.10%. Furthermore, higher error suggests that parallel printed samples have lower reproducibility with the method presented in this work. Nevertheless, the C group exhibited a slightly lower mean response time of 0.60 ± 0.08 s compared to 0.69 ± 0.04 s for the B group. This, together with the lower recovery time of the B group (14.17 ± 1.64 s) compared to the C group (15.93 ± 1.12 s), further highlights the anisotropy of the material. As a highlight, both samples in Fig. 5c displayed drift, which is common

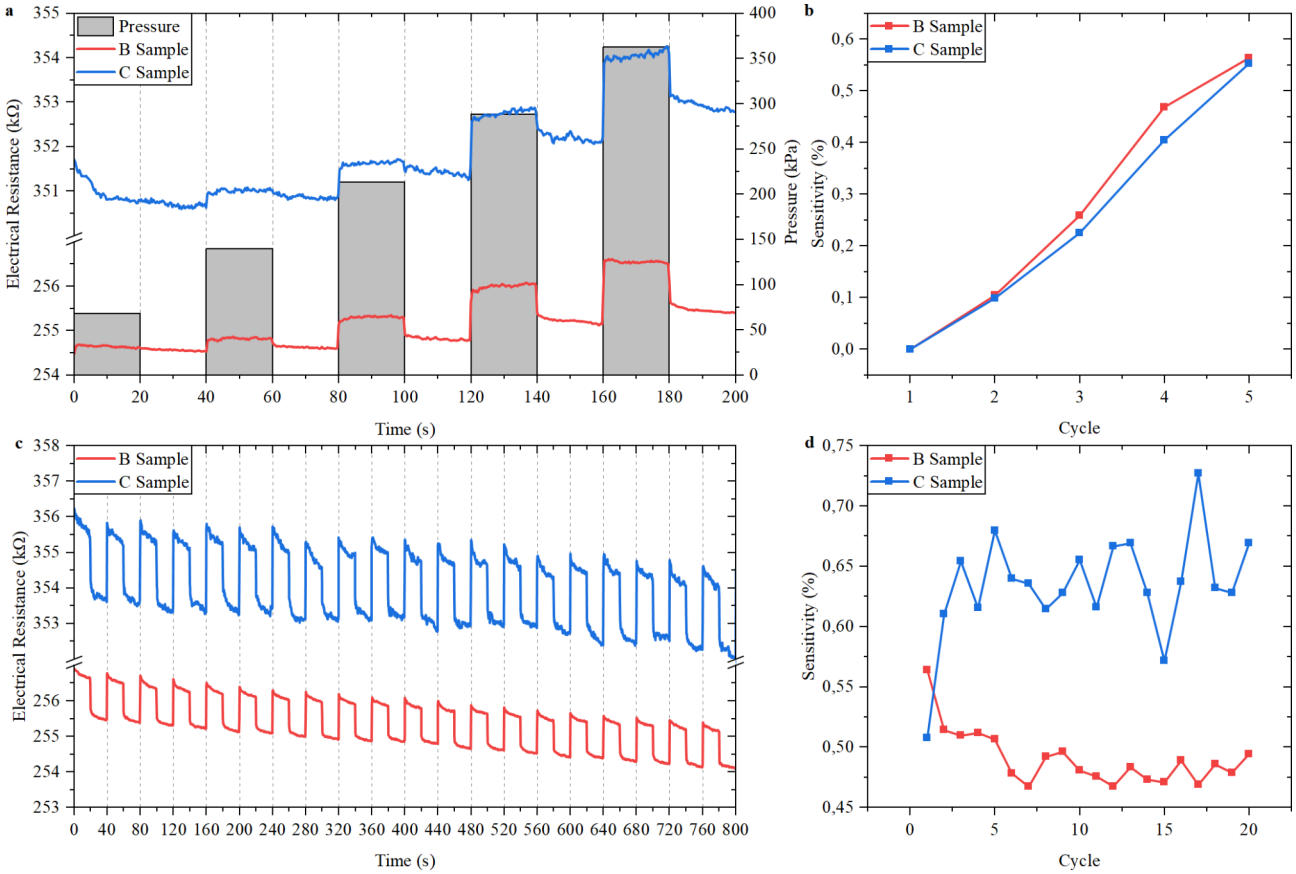

Fig. 5. Anisotropic piezoresistive behavior. (**a**) piezoresistive response of a group B and a group C sample in cycles of 20 s of load followed by 20 s without it, applying pressures ranging from 68.27 ± 0.22 kPa to 363.25 ± 0.39 kPa, with a mean increase of 73.89 ± 1.60 kPa per cycle. (**b**) sensitivity of the same individual group B and C samples per load cycle showing a quasi-linear response to increasing pressure. (**c**) piezoresistive response of a group B and a group C sample in cycles of 20 s of load followed by 20 s without it, applying a fixed pressure of 363.25 ± 0.39 kPa per cycle. (**d**) sensitivity of the same B and C samples over 20 cycles, highlighting continuous variations in sensitivity for C sample and tendency of stabilization of the B sample signal, despite its degradation. The preparation process resulted in anisotropic piezoresistive response, with different electrical resistances in function of the printing lines direction. This also resulted in more noise in the C sample signal and distinguishable behavior between groups for 20 cycles for the two individual samples analyzed.

for CNTs-based nanostructured sensors as some factors affect the electrical behavior of the nanotubes, such as the temperature[48,49]. This effect possibly can be minimized by controlling the measuring voltage and using programable microcontrollers to calibrate the sensor[49,50].

Additionally, Fig. 5d illustrates the sensitivity over 20 pressure cycles with same load for each individual samples. The results indicate variations in sensitivity over the cycles, which can be attributed to plastic deformations on the ABS substrate and damage to the CNTs film due to mechanical stress. This effect was particularly pronounced in the C sample, which exhibited erratic sensitivity behavior. Notably, the B sample showed a tendency to stabilize after an initial drop in sensitivity, suggesting that the samples could operate for more cycles with reduced performance.

Discussion

The deposition of a solution of carbon nanotubes by pulverization with an aerograph over an ABS polymer substrate resulted in a piezoresistive nanostructured film as the material percolated and reached electrical resistances around 10^6 W, usable in conventional electronic circuits. The random arrangement of CNTs on parallel and perpendicular 3D-printed ABS substrates observed in FEG-SEM micrographs explains the piezoresistive behavior, as mechanical stress on the polymer affects the nanotubes conduction channels. Furthermore, a micrograph indicates that the CNTs appears to be fused to the polymer substrate in the first layer, suggesting the formation of a nanocomposite. Raman spectroscopy reveals that the CNTs appear compressed and subjected to p-type doping due to their distribution and interaction with the ABS substrate, potentially contributing to the piezoresistivity and corroborating the formation of a nanocomposite.

The presented method resulted in sensor elements with a maximum sensitivity of 0.75 ± 0.36% for a CNTs mass percentage of 0.22 ± 0.30%, achieving a functional material with promising industrial scalability. Although some CNTs-based piezoresistive nanocomposites reach sensitivities around 10%[21], 80%[27] and 1%[29], they need respectively about 1.2 ~ 2, 4 ~ 8 and 6 wt% of nanotubes, besides using more complex preparation methods. Apart from the simplicity, the pulverization method also shows promise for usage with other 3D printing materials, such as TPU which is more elastic than ABS and could deform more, potentially displaying higher sensitivity and broader operational range.

The best-performing sensing elements were from group B, with parallel printing lines and applied electric field during preparation, which exhibited better overall repeatability and higher mean sensitivity. This superior performance is attributed to fewer printing defects and more homogeneous nanostructured films, as evidenced by FEG-SEM micrographs. However, the orientation of the printing lines induced anisotropy in the piezoresistive response, with the C samples displaying higher mean electrical resistance and increased signal noise. This anisotropy can be controlled through 3D printing and electric field during production, allowing the material to be tailored, for example, to distinguish directions of mechanical tension. To achieve this, the sensing elements could be redesigned to have four terminals to simultaneously measure the resistance parallel and perpendicular to the printing lines or to have two layers of CNTs, one for each orientation.

To further improve these results, 3D printing offers many possibilities of implementation designs, such as developing on-demand devices that allow greater deformation of the sensing element for increased sensitivity or restrict pressure transmission in high-load scenarios. Moreover, the usage of IoT-ready microcontrollers, such as the ESP32, could be useful to calibrate and minimize the drift issue observed during pressure cycles. Given the operational range achieved, between 139.97 ± 0.46 to 363.25 ± 0.39 kPa, the material could be used for example in flexible wearable motion monitor and robotics applications. For instance, the material is being evaluated for integration into a haptic feedback system in a robot's wheel designed for industrial inspection, aiming to acquire terrain information through an integrated pressure sensor with IoT. In this case, the piezoresistive response could indicate the wheel's contact with the ground and variations in pressure from different soils. Furthermore, the anisotropy could help distinguish other forces, such as lateral loads during curves and torque-induced loads on the wheels.

Methods

Material preparation

The filament used was a commercial translucent ABS with 1.75 mm of diameter. The acetone and the N, N-dimethylformamide were of 99.5% and 99.8% of purity, respectively. The MWCNTs-COOH with 99.80% of purity were purchased from Federal University of Acre, Brazil, where they were synthetized by CVD at 750 °C, purified and treated in acid reflux in a solution of 3:1 of HNO_3/H_2SO_4 for functionalization.

ABS/Acetone solution preparation

The solution was prepared with ABS (5 g) filament parts cut with approximate length of 4 mm added to acetone (25 ml). The solution put in a model Q21L ultrasonic washer (Ultronique) for an hour at 40 kHz in ambient temperature, until the polymer was solubilized.

Acetone-DMF/MWCNTs-COOH solution preparation

The solution was prepared with as received flakes of MWCNTs-COOH (20 mg) added to acetone (10 ml) and DMF (10 ml). For better dispersion, the solution was ultrasonicated on a model L100 ultrasonic washer (Schulster) for an hour and 20 min, at 42 kHz in ambient temperature.

3D printing of ABS sensor elements

The 3D model of the samples was designed on Inventor (Autodesk) with 25 mm of length, 5 mm of width (7 mm in central region) and 0.8 mm of height. PrusaSlicer (Prusa) was used to slice the model for 3D printing and adjust parameters, such as the temperature defined to 220 °C and printing speed defined to 10 mm/s. The models were sliced with printing lines in two directions, one parallel to the largest length of the sensing elements and the other perpendicular to this length. The sensor elements were produced using translucent ABS filament with 1.75 mm of diameter in a Stella 3 Lite 3D printer (Boa Impressão 3D) with a 0.2 mm nozzle.

Preparation of ABS/COOH-MWCNT sensor elements

The nanostructured sensor elements were prepared by the manual pulverization of the Acetone-DMF/MWCNTs-COOH solution using an Vonder aerograph at about 10 cm from the samples. This process was made inside a fume hood at ambient temperature. Layers of CNTs were applied in cycles of pulverization, 10 min of drying and 10 electrical resistance measurements. To try to align the CNTs and improve its adhesion on the ABS substrate, half of the samples were subjected to 500 V (electric field of approximately 38.5 kV/m) for about 0.334 s after the pulverization. After a week, new electrical measurements were made. To finalize the production, the ends of the samples were covered with conductive silver ink to be used as electrical terminals and the ABS/Acetone solution was applied to its center with a pipette to act as a sealing layer of ABS after the evaporation of the solvent.

Morphological characterization

Six samples were prepared with a progressive number of layers of CNTs and without the sealing layer to be analyzed by Field Emission Gun Scanning Electron Microscopy using a MIRA 3 microscope (TESCAN). Due to the polymeric substrate, the equipment was operated at 5 kV to prevent damage to the material. The samples were also fixed on the stubs with conductive carbon tape and grounded with conductive silver ink to avoid electrical charge accumulation.

Raman spectroscopy characterization

The vibrational analysis was made with a LabRAM HR Evolution Raman spectrometer (Horiba Scientific) using a laser with 633 nm wavelength and 9.46 mW power with a 20x magnification objective lens. The spectra were obtained with 2 accumulations and 120 s accumulation time, from 900 to 3200 cm^{-1}.

Electrical characterization

The electrical resistance measurements were made with a model 6487 picoammeter (Keithley Instruments) using the two-point method with a 237-ALG-2 cable. The data was acquired using programming lines written in Python to send SCPI codes to the equipment via a RS-232 cable. The measurements were made using 10 V in three situations: between the cycles of CNTs pulverization; over five load cycles with progressive pressure; and over 20 load cycles with constant pressure. The pressure was applied by controlling the height of an actuator, which applied 73.89 ± 1.60 kPa per 0.1 mm variation. The progressive pressure cycles were made with motions from 0.2 mm to 1 mm in 0.2 mm steps, resulting in an initial pressure of 68.27 ± 0.22 kPa and a final one of 363.25 ± 0.39 kPa, limited by the geometry of the 3D printed device. The constant pressure cycles were made with a 363.25 ± 0.39 kPa load. In each cycle there were 20 s with pressure and 20 s without it, with continuous data acquisition in approximately 0.334 s intervals.

Data availability

The authors declare that the data supporting the findings of this study are available within the paper and its supplementary information.

Received: 16 July 2024; Accepted: 9 October 2024
Published online: 25 October 2024

References

1. Baig, N., Kammakakam, I. & Falath, W. *Mater. Adv.* **2**, 1821–1871 (2021).
2. Souza, F. G. Jr. et al. A 30-year review on nanocomposites: Comprehensive bibliometric insights into microstructural, electrical, and mechanical properties assisted by artificial Intelligence. *Materials* **17**, 1088 (2024).
3. Speranza, G. Carbon nanomaterials: Synthesis, functionalization and sensing applications. *Nanomaterials* **11**, 967 (2021).
4. Cheng, G. et al. Carbon nanotubes field-effect transistor pressure sensor based on three-dimensional conformal force-sensitive gate modulation. *Carbon* **204**, 456–464 (2023).
5. Kouediatouka, A. N. et al. Carbon nanotube/liquid metal hybrid coating-based flexible pressure piezoresistive sensors. *Chem. Eng. J.* **481**, 148637 (2024).
6. Ma, L. & Lu, W. Carbon nanotube film based flexible bi-directional strain sensor for large deformation. *Mater. Lett.* **260**, 126959 (2020).
7. Hu, X. et al. A super-stretchable and highly sensitive carbon nanotube capacitive strain sensor for wearable applications and soft robotics. *Adv. Mater. Technol.* **7**, 2100769 (2022).
8. Rao, R. K. & Sasmal, S. Smart nano-engineered cementitious composite sensors for vibration-based health monitoring of large structures. *Sens. Actuators A* **311**, 112088 (2020).
9. Jeong, C. et al. Bioinspired, high-sensitivity mechanical sensors realized with hexagonal microcolumnar arrays coated with ultrasonic-sprayed single-walled carbon nanotubes. *ACS Appl. Mater. Interfaces* **12**, 18813–18822 (2020).
10. Tang, Z. et al. Comprehensive evaluation of the piezoresistive behavior of carbon nanotube-based composite strain sensors. *Compos. Sci. Technol.* **208**, 108761 (2021).
11. Kanoun, O. et al. Review on conductive polymer/CNTs nanocomposites based flexible and stretchable strain and pressure sensors. *Sensors* **21**, 341 (2021).
12. Jorio, A., Dresselhaus, G. & Dresselhaus, M. S. (eds) *Carbon Nanotubes: Advanced Topics in the Synthesis, Structure, Properties and Applications* (Springer, 2008).
13. Sonkar, P. K., Kumar, N. & Gupta, P. K. *Fundamentals and Properties of Multifunctional Nanomaterials Ch. 5* (Elsevier, 2021).
14. Lavagna, L. el al. Functionalization as a way to enhance dispersion of carbon nanotubes in matrices: A review. *Mater. Today Chem.* **20**, 100477 (2021).
15. Dubey, R. et al. Functionalized carbon nanotubes: Synthesis, properties and applications in water purification, drug delivery, and material and biomedical sciences. *Nanoscale Adv.* **3**, 5722 (2021).
16. Wang, B. & Pang, B. The influence of N,N-Dimethylformamide on dispersion of multi-walled carbon nanotubes. *Russ. J. Phys. Chem. A* **94**, 810–817 (2020).
17. Lu, T. & Chen, W. Material recycling of acrylonitrile butadiene styrene (ABS) from toy waste using density separation and safer solvents. *Resour. Conserv. Recycl.* **197**, 107090 (2023).
18. Podsiadły, B. et al. Carbon nanotube-based composite filaments for 3D printing of structural and conductive elements. *Appl. Sci.* **11**, 1272 (2021).
19. Eisape, A. et al. Soft CNT-polymer composites for high pressure sensors. *Sensors* **22**, 5268 (2022).
20. Zhang, S. et al. Enhanced piezoresistive performance of conductive WPU/CNT composite foam through incorporating brittle cellulose nanocrystal. *Chem. Eng. J.* **387**, 124045 (2020).
21. Li, Q., Luo, S. & Wang, Q. Piezoresistive thin film pressure sensor based on carbonnanotube-polyimide nanocomposites. *Sens. Actuators A* **295**, 336–342 (2019).
22. Mitrakos, V. et al. Nanocomposite-based microstructured piezoresistive pressure sensors for low-pressure measurement range. *Micromachines* **9**, 43 (2018).
23. Sanati, M. et al. Development of nanocomposite-based strain sensor with piezoelectric and piezoresistive properties. *Sensors* **18**, 3789 (2018).
24. Sanli, A., Ramalingame, R. & Kanoum, O. Piezoresistive pressure sensor based on carbon nanotubes/epoxy composite under cyclic loading. In *2018 IEEE International Instrumentation and Measurement Technology Conference* 1–5 (2018).
25. Hosseini, S., Norouzi, M. & Xu, J. A. Sensitive strain sensor based on multi-walled carbon nanotubes/polyaniline/silicone rubber nanocomposite for human motion detection. *Sci* **5**, 36 (2023).
26. Ma, L. et al. A 3D-printed, sensitive, stable, and flexible piezoresistive sensor for health monitoring. *Adv. Eng. Mater.* **23**, 2100379 (2021).
27. Verma, P. et al. Multifunctional characteristics of 3D printed polymer nanocomposites under monotonic and cyclic compression. *Def. Technol.***30**, 13–22 (2023).

28. Xiang, D. et al. Effects of non-covalent interactions on the properties of 3D printed flexible piezoresistive strain sensors of conductive polymer composites. *Compos. Interfaces* **28**, 577–591 (2021).
29. Dul, S., Pegoretti, A. & Fambri, L. Fused filament fabrication of piezoresistive carbon nanotubes nanocomposites for strain monitoring. *Front. Mater.* **7** (2020).
30. Yin, Z. et al. The relevant approaches for aligning carbon nanotubes. *Micromachines* **13**, 1863 (2022).
31. Gao, J., He, Y. & Gong, X. Effect of electric field induced alignment and dispersion of functionalized carbon nanotubes on properties of natural rubber. *Results Phys.* **9**, 493–499 (2018).
32. Sanivada, U. et al. Joule-heating effect of thin films with carbon-based nanomaterials. *Materials* **15**, 4323 (2022).
33. Sangroniz, L. et al. Matching rheology, conductivity and joule effect in PU/CNT nanocomposites. *Polymers* **13**, 950 (2021).
34. Collins, P. G. et al. Extreme oxygen sensitivity of electronic properties of carbon nanotubes. *Science* **287**, 1801–1804 (2000).
35. Goldoni, A. et al. Single-wall carbon nanotube interaction with gases: Sample contaminants and environmental monitoring. *J. Am. Chem. Soc.* **125**, 11239–11333 (2003).
36. Bikulčius, G., Ignatjev, I. & Ručinskienė, A. Rapid method to determine suitability of ABS plastics for metallization. *Trans. IMF* **92**, 47–51 (2014).
37. Tympa, L. et al. Do microplastics enter our food chain via root vegetables? A Raman based spectroscopic study on *Raphanus sativus*. *Materials* **14**, 2329 (2021).
38. Larkin, P. J. *Infrared and Raman Spectroscopy: Principles and Spectral Interpretation* (Elsevier, 2011).
39. Dresselhaus, M. S. et al. Raman spectroscopy of carbon nanotubes. *Phys. Rep.* **409**, 47–99 (2005).
40. Reis, M. A. L. et al. Raman spectroscopy fingerprint of stainless steel-MWCNTs nanocomposite processed by ball-milling. *AIP Adv.* **8**, 015323 (2018).
41. Zhao, X. et al. Multiple splitting of G-band modes from individual multiwalled carbon nanotubes. *Appl. Phys. Lett.* **81**, 2550 (2002).
42. Saito, R. et al. First and second-order resonance raman process in graphite and single wall carbon nanotubes. *Jpn J. Appl. Phys.* **41**, 4878–4882 (2002).
43. Antunes, E. F. et al. Comparative study of first- and second-order Raman spectra of MWCNT at visible and infrared laser excitation. *Carbon* **44**, 2202–2211 (2006).
44. Rebelo, S. L. H. et al. Progress in the Raman spectra analysis of covalently functionalized multiwalled carbon nanotubes: Unraveling disorder in graphitic materials. *Phys. Chem. Chem. Phys.* **18**, 12784–12796 (2016).
45. Lee, J. E. et al. Optical separation of mechanical strain from charge doping in graphene. *Nat. Commun.* **3**, 1024 (2012).
46. Li, Z. et al. Raman spectroscopy of carbon materials and their composites: Graphene, nanotubes and fibres. *Prog. Mater. Sci.* **135**, 101089 (2023).
47. Jorio, A. & Saito, R. Raman spectroscopy for carbon nanotube applications. *J. Appl. Phys.* **129**, 021102 (2021).
48. Devi, R. & Gill, S. Performance investigation of carbon nanotube based temperature compensated piezoresistive pressure sensor. *Silicon* **14**, 3931–3938 (2022).
49. Noyce, S. et al. Electronic stability of carbon nanotube transistors under long-term bias stress. *Nano Lett.* **19**, 1460–1466 (2019).
50. Martínez, J. et al. Self-calibration technique with lightweight algorithm for thermal drift compensation in MEMS accelerometers. *Micromachines* **13**, 584 (2022).

Acknowledgements

The authors would like to thank CAPES and Finep (grant number: 01.22.0133.00) for the financial support. The authors also thank the Laboratory of Vibrational Spectroscopy and High Pressures (LEVAP) from Federal University of Pará (UFPA) and the Electronic Microscopy Laboratory (LME) of Pará Museum Emílio Goeldi (MPEG) for supporting respectively the Raman spectroscopy and the FEG-SEM characterizations. Soli Deo Gloria.

Author contributions

M.R. and L.Q. conceptualized and designed the study. L.Q., D.O., and R.D. prepared the sensing element samples. L.Q. and R.D. performed the electrical data acquisition. K.A. and L.Q. performed the FEG-SEM and Raman spectroscopy data acquisition. L.Q. and M.R. performed the data treatment and analysis. L.B., G.P., A.S., and W.P. reviewed the data and discussed the results. L.Q. wrote the original draft and M.R. made the main revision of the manuscript. All authors have reviewed and approved the manuscript.

Declarations

Competing interests

The authors declare no competing interests.

Additional information

Supplementary Information The online version contains supplementary material available at https://doi.org/10.1038/s41598-024-76028-2.

Correspondence and requests for materials should be addressed to L.J.B.Q.

Reprints and permissions information is available at www.nature.com/reprints.

Publisher's note Springer Nature remains neutral with regard to jurisdictional claims in published maps and institutional affiliations.